



HAL
open science

Stability of $\text{Cu}(\text{In}_x \text{Ga}_{1-x})\text{Se}_2$ Solar Cells Utilizing RbF Postdeposition Treatment under a Sulfur Atmosphere

Jake Wands, Alexandra Bothwell, Polyxeni Tsoulka, Thomas Lepetit, Nicolas Barreau, Angus Rockett

► **To cite this version:**

Jake Wands, Alexandra Bothwell, Polyxeni Tsoulka, Thomas Lepetit, Nicolas Barreau, et al.. Stability of $\text{Cu}(\text{In}_x \text{Ga}_{1-x})\text{Se}_2$ Solar Cells Utilizing RbF Postdeposition Treatment under a Sulfur Atmosphere. *Advanced Energy and Sustainability Research*, In press, 4 (11), pp.2300052. 10.1002/aesr.202300052 . hal-04163423

HAL Id: hal-04163423

<https://hal.science/hal-04163423>

Submitted on 17 Jul 2023

HAL is a multi-disciplinary open access archive for the deposit and dissemination of scientific research documents, whether they are published or not. The documents may come from teaching and research institutions in France or abroad, or from public or private research centers.

L'archive ouverte pluridisciplinaire **HAL**, est destinée au dépôt et à la diffusion de documents scientifiques de niveau recherche, publiés ou non, émanant des établissements d'enseignement et de recherche français ou étrangers, des laboratoires publics ou privés.

Stability of $\text{Cu}(\text{In}_x\text{Ga}_{1-x})\text{Se}_2$ Solar Cells Utilizing RbF Postdeposition Treatment under a Sulfur Atmosphere

Jake Wands,* Alexandra Bothwell, Polyxeni Tsoulka, Thomas Lepetit, Nicolas Barreau, and Angus Rockett

Alkali halide postdeposition treatments (PDTs) have become a key tool to maximize efficiency in $\text{Cu}(\text{In}_x\text{Ga}_{1-x})\text{Se}_2$ (CIGS) photovoltaics. RbF PDTs have emerged as an alternative to the more common Na- and K-based techniques. This study utilizes temperature-dependent current–voltage (*JVT*) measurements to study a unique RbF PDT performed in a S atmosphere. The samples are measured before and after 6 months in a desiccator to study device stability. Both samples contain Na and K which diffuse from the soda–lime glass substrate. A reference sample and a RbF + S PDT sample both show the development of a rear contact barrier after aging. The contact barrier is higher for the RbF + S PDT sample, leading to decreased current in forward bias. Series resistance is also higher in the RbF + S PDT device which leads to lower fill factor. However, after aging the reference sample has a larger decrease in open-circuit voltage (V_{OC}). Ideality factor measurements suggest Shockley–Read–Hall recombination dominates both samples. V_{OC} versus temperature and a temperature-dependent activation energy model are used to calculate diode activation energies for each sample condition. Both techniques produce similar values that indicate recombination primarily occurs within the bulk absorber.

1. Introduction

$\text{Cu}(\text{In}_x\text{Ga}_{1-x})\text{Se}_2$ (CIGS) photovoltaics are one of the most successful thin-film technologies, with a record cell efficiency of 23.4%.^[1] Key to the performance of modern CIGS devices is the use of alkali halide postdeposition treatments (PDTs).^[2] These treatments most commonly utilize Na or K as the alkali metal; however, Rb and Cs have also shown potential benefits.^[3,4] RbF has received increased attention in recent years due to potential open-circuit voltage (V_{OC}) improvements over Na and K.^[5] However, there are still questions about the stability of RbF PDT devices which need to be addressed before commercial use. In addition, PDT treatments are often performed in a Se atmosphere, although little study into the influence of other chalcogens on device performance has been conducted.^[6]

In this work, we report the aging effects of a device with RbF PDT performed in a S atmosphere compared to an untreated reference, investigated using temperature-dependent current–voltage (*JVT*) measurements. Series resistance was found to contribute to reduced fill factor (FF), and the effect grew larger over time. A back barrier, modeled as a second diode with reverse polarity, was shown to form in both devices, although the barrier height was greater in the RbF + S PDT sample. Each sample indicates that bulk recombination via a Shockley–Read–Hall (SRH) mechanism dominated recombination. The PDT proved to be an effective method of improving V_{OC} ; however, the efficiency suffered after aging. Improving the long-term stability will be necessary for the commercial viability of this technique.

2. Experimental Section


The samples used in this study were complete solar cell devices with a layer stack consisting of: soda–lime glass/Mo/CIGS/PDT/CdS/ZnO/ZnO:Al/metallic grids, where PDT refers to a PDT step performed between the CIGS and CdS depositions. The reference device received no PDT step, while a RbF + S PDT was used in the second device. For the remainder of this article these samples will be referred to as Ref and RbF(S) PDT, respectively. The CIGS absorber layer was deposited by a three-stage coevaporation process and designed to achieve a graded bandgap, higher

J. Wands, A. Rockett
Department of Metallurgical and Materials Engineering
Colorado School of Mines
1500 Illinois St, Golden, CO 80401, USA
E-mail: jwands@mines.edu

A. Bothwell
Materials, Chemical, and Computational Sciences Department
National Renewable Energy Laboratory
15013 Denver West Pkwy, Golden, CO 80401, USA

P. Tsoulka, T. Lepetit, N. Barreau
Nantes Université
CNRS

Institut des Matériaux de Nantes Jean Rouxel
IMN
F-44000 Nantes, France

 The ORCID identification number(s) for the author(s) of this article can be found under <https://doi.org/10.1002/aesr.202300052>.

© 2023 The Authors. Advanced Energy and Sustainability Research published by Wiley-VCH GmbH. This is an open access article under the terms of the Creative Commons Attribution License, which permits use, distribution and reproduction in any medium, provided the original work is properly cited.

DOI: 10.1002/aesr.202300052

at the front and rear. The final film composition was copper poor with a ratio of copper to group III elements of 0.95. The PDT was performed by coevaporation of elemental sulfur (120 nm min^{-1}) and RbF (3 nm min^{-1}) at a substrate temperature of $350 \text{ }^\circ\text{C}$ to achieve a 15 nm -thick layer. CdS was added by chemical bath deposition and the ZnO/ZnO:Al bilayer was rf-sputtered. Finally, electron beam evaporation was used to deposit the metallic grids through a shadow mask. More details on the device fabrication process can be found in ref. [6]. Device measurements were performed on the samples shortly after deposition (referred to as fresh) as well as after 6 months storage in a desiccator in the dark (referred to as aged). No light soaking procedure was used.

External quantum efficiency (EQE) spectra were measured from 300 to 1400 nm using an Oriel 200 system with no external illumination or voltage bias applied. JVT experiments were performed from 350 to 180 K in 10 K increments. The voltage was swept from -0.5 to 2 V with the current limited to 800 mA . A solar simulator producing a simulated AM1.5 spectrum calibrated to 100 mW cm^{-2} was used for illuminated measurements. Light and dark data were compared to detect light-dependent changes in the device and bias-dependent collection. JVT measurements were taken on each device immediately after manufacture and 6 months later after storage in a desiccator.

To extract the reverse saturation current (J_0) and ideality factor (n) values, the impacts of shunt (R_{SH}) and series (R_S) resistance must be accounted for. This was done by first calculating the differential resistance (dV/dJ) for each JV curve. The region of the dV/dJ curve with a linear, negative slope on a semilog plot is dominated by the resistance of the main diode. Without

including these, the ideality factor is overestimated with a corresponding error in reverse saturation current. It is important where this region covers a narrow voltage and current range to account simultaneously for the series and shunt resistances. An example dV/dJ curve is presented in the Supporting Information (SI) Figure 1. A linear equation was fit to the main diode region of the dV/dJ curve and used to calculate dV/dJ as a function of voltage. The voltage step between data points, dV , was divided by dV/dJ to calculate the dJ curve for the main diode. Finally, the dJ values were integrated over the desired voltage range to produce the main diode JV curve. J_0 and n parameters were calculated from the intercept and slope, respectively, of a linear curve fit to the data on a semilog plot.^[7]

3. Results and Discussion

Device performance parameters at 300 K are provided in Table 1 along with the change in value after the 6 month period. When the samples were fresh, V_{OC} improved after RbF + S PDT in agreement with many existing studies on RbF PDTs, indicating that the presence of S did not negate this beneficial outcome.^[4-6,8] Short-circuit current (J_{SC}) was similar between the two samples with the RbF(S) PDT experiencing a minor drop. FF declined slightly in the fresh RbF(S) device relative to the Ref sample. The impact of RbF PDT on FF is mixed in the literature with some results showing little effect or small increases.^[4,5,8] A previous study on the RbF + S PDT also showed a small decrease in FF, but further investigations may be necessary to be definitive.^[6]

While each device saw a drop in overall efficiency, the source of decline was different. The Ref sample degraded most in V_{OC} relative to the PDT sample. A modest decline in J_{SC} was seen in the Ref sample, while the RbF(S) PDT device had a more noticeable decrease. EQE measurements before and after aging show that the Ref device experienced relatively small declines across the measurement range (Figure 1). The RbF(S) PDT device lost current primarily at higher energies, which may indicate reduced collection near the junction.

The Ref sample lost 5 abs\% of FF, which is significant but less than the 9 abs\% drop in the RbF(S) PDT sample. R_S had a notable impact on the FF of each device, particularly after aging and at low temperatures. The effect of series resistance can be deconvoluted from FF using Equation (1) where FF_0 is the FF with series resistance removed and FF_S is the measured FF ^[9]

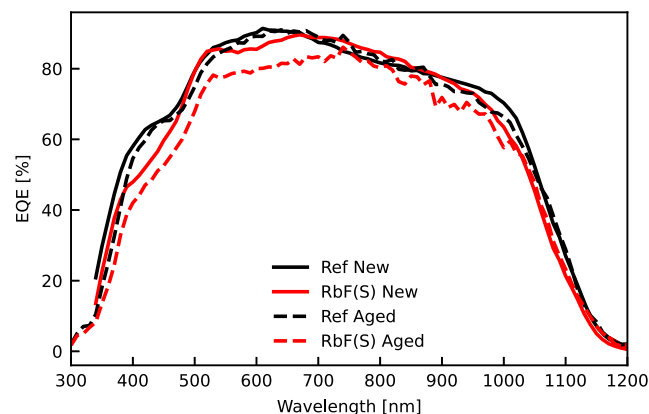


Figure 1. EQE measurements show reduction at low energies (Ref) and high energies (RbF(S) PDT), respectively, after aging.

Table 1. JV parameters, R_S , and its impact on FF before and after aging for each device.

		V_{OC} [mV]	J_{SC} [mA cm^{-2}]	FF [%]	η [%]	R_S [$\Omega \text{ cm}^2$]	FF_0 [%]	FF deficit [abs%]
Ref	Fresh	678	32.8	74.4	16.5	0.92	77.8	3.5
	Aged	622	32.7	69.3	14.1	1.42	74.9	5.6
	Change	-56	-0.1	-5	-2.4	+0.5		+2.1
RbF(S) PDT	Fresh	712	32.2	72.5	16.6	1.40	77.4	4.9
	Aged	679	30.0	63.1	12.9	2.30	70.2	7.1
	Change	-33	-2.2	-9	-3.7	+0.9		+2.2

$$FF_0 = FF_S \left(1 - \frac{J_{SC}}{V_{OC}} R_S \right)^{-1} \quad (1)$$

The difference between these two values is referred to here as the FF deficit. FF deficits for each device can be found in Table 1 and show a notable increase after aging. As the RbF(S) PDT device had a larger increase in R_S after aging, it also saw a larger increase in FF deficit. Similar calculations were performed for the effect of R_{SH} on FF, but the R_{SH} values for each device were large enough to make the impact negligible.

Semilog JV plots at 200 and 300 K in the dark are shown in **Figure 2** (for complete JVT plots, see Figure S2, Supporting Information). A notable development was the formation of a low-temperature blocking contact after aging which was not present in the fresh samples. This is most obvious in the 200 K plots

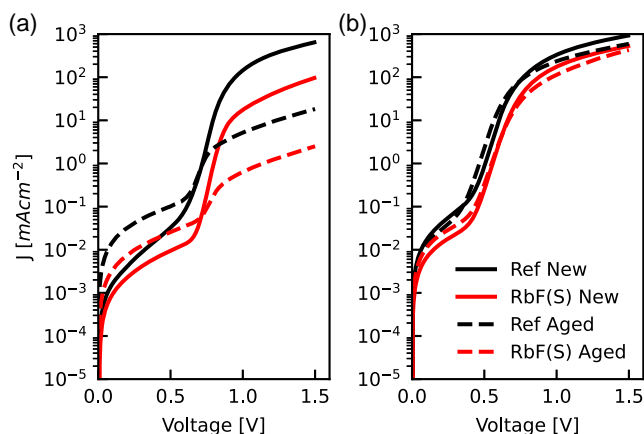


Figure 2. Semilog JV curves measured at a) 200 K and b) 300 K for each device before and after aging.

where the current at forward bias voltages above 1 V was reduced after aging, indicating a barrier had developed.

A roll-over effect in CIGS solar cells has previously been attributed to a Schottky diode forming at the back contact with opposite polarity to the main junction.^[10–12] The applied bias is therefore split between the two diodes and the series resistance as depicted in the equivalent circuit diagram in **Figure 3a**. As the current through both diodes must be the same, the main diode bias, V_m , can be estimated using the full device current, and the main diode JV curve calculated with the dV/dJ analysis. The bias across the back diode can then be calculated by^[13]

$$V_b = V_{\text{applied}} - V_m - JR_S \quad (2)$$

where V_{applied} is the bias across the whole device and R_S is the series resistance. The voltage split between V_m and V_b can be found in Figure S3, Supporting Information. Now the JV curve of the back diode can be plotted as J versus V_b as shown in Figure 3b. Because the back diode has opposite polarity, the plot depicts reverse leakage current when the net current is positive (first quadrant of the JV plot). The Ref device exhibited higher leakage current in the blocking diode compared to the RbF(S) PDT sample. As the back diode blocks current flow, the high leakage current in the Ref sample was beneficial. In other words, the aging process produced a stronger blocking diode in the RbF(S) PDT device.

The back barrier height for each device can be estimated using^[11]

$$J_{\text{limit}} = A^* T^2 e^{-\frac{q\phi_b}{kT}} \quad (3)$$

where J_{limit} is the current density at which rollover begins, T is the temperature, q is the electronic charge, k is the Boltzmann constant, ϕ_b is the back barrier height, and A^* is the Richardson constant described by

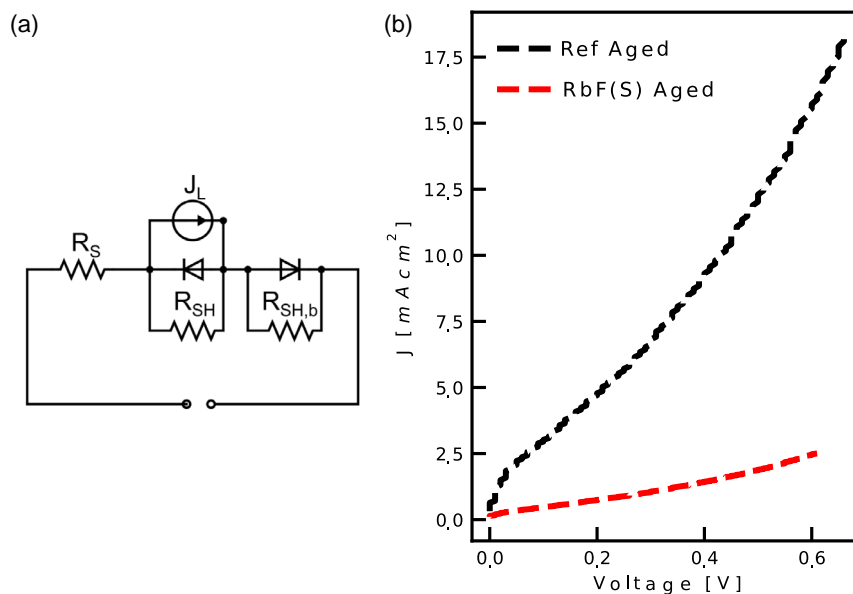


Figure 3. a) Equivalent circuit diagram depicting the reverse polarity rear diode and b) JV curves for the reverse polarity back diode in the aged devices at 200 K.

$$A^* = \frac{4\pi q m^* k^2}{h^3} \quad (4)$$

In this case, m^* is the effective mass of holes and h is Planck's constant. The barrier height was calculated to be 381 and 402 meV for the Ref and RbF(S) PDT devices, respectively. Although the cause of this increased barrier in the RbF(S) PDT device is not known, time-of-flight secondary ion mass spectroscopy (TOF-SIMS) depth profiles of the aged samples (included in Supporting Information) showed a spike in alkali elements at the back contact. The Ref sample had a large increase in Na and K at the rear contact, while the increase in the RbF(S) PDT device was reduced. The Na and K likely diffused into the sample from the glass substrate. The RbF(S) PDT device had a significant spike in Rb at the back contact which appears to have excluded Na and K ions from the region. This ion exchange has been observed previously and is confirmed in the samples studied here.^[8,14]

Ideality factor versus temperature is shown for each device in **Figure 4** extracted after accounting for the series and shunt resistances. The fresh devices both showed ideality factors in the range of 1.4–1.5 at temperatures above 250 K. These values are indicative of SRH recombination through states that are located between the band-edge and midgap.^[7] Before aging there was a gradual rise in ideality factor at low temperatures, which was more pronounced in the Ref sample than the RbF(S) sample. The ideality factor rise above two in the Ref sample could result from tunneling recombination or interface effects.^[7,15] The aging process had relatively small impacts on ideality factor of the Ref device and suggests SRH recombination still dominated for $T > 250$ K. In the RbF(S) PDT device, the ideality factor was consistently higher after aging, although the values remained under two for most of the temperature range.

JVT data can be further analyzed to calculate the diode activation energy (E_a) using the reverse saturation current density (J_0) as a function of temperature.^[16] The activation energy provides information about the dominant recombination mechanism in a device. If $E_a \approx E_g$, recombination primarily occurs within the bulk absorber, while $E_a < E_g$ occurs when interface recombination is dominant. While this technique is common in the literature, activation energy is typically calculated from the slope of a $\ln(J_0)$ versus $1/kT$ or $\ln(J_0/T^{2.5})$ versus $1/kT$ plot. These models may be

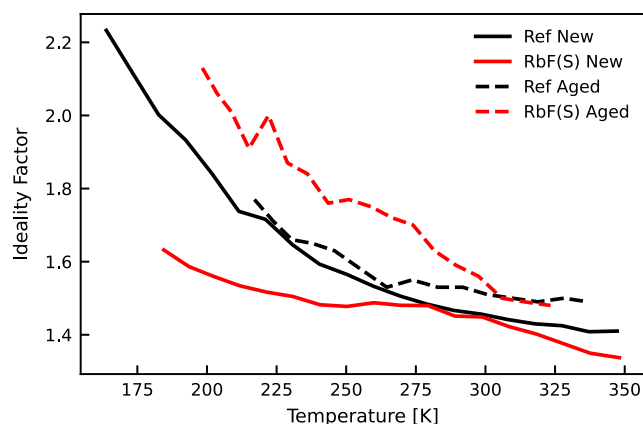


Figure 4. Ideality factor as a function of temperature for each device.

appropriate in some samples, but they assume that ideality factor and activation energy are temperature independent. As shown in **Figure 4**, the ideality factor in these devices has a moderate temperature dependence which needs to be accounted for.

A more robust analysis of J_0 can be performed by considering temperature dependent ideality factors.^[17]

$$J_0 = J_{00} \exp\left(-\frac{E_a}{n(T)kT}\right) \quad (5)$$

$$n(T) \ln\left(\frac{J_0}{J_{00}}\right) = -\frac{E_a}{kT} \quad (6)$$

Based on Equation (6), a plot of $n(T) \ln(J_0/J_{00})$ versus $1/kT$ will yield the activation energy, as shown in **Figure 5**. The activation energy values are listed in **Table 2**. Each activation energy was close to the CIGS bandgap (≈ 1.15 eV), which generally indicates that recombination in the bulk dominates current flow rather than at interfaces. This may indicate that the ideality factor values above two at low temperature were related to tunneling effects rather than interface recombination. The slight decrease in activation energy after aging for the Ref device may suggest that interface recombination begins to have more influence after aging.

To verify that the ideality factor is the only additional temperature dependent variable, Equation (6) can be rearranged

$$\ln\left(\frac{J_0}{J_{00}}\right) = -\frac{E_a}{n(T)kT} \quad (7)$$

Using Equation (7), an additional plot of $\ln(J_0/J_{00})$ versus $1/n(T)kT$ can be used which should yield the same activation energy if $n(T)$ is the only temperature dependent term.

As shown in **Figure 6**, this method did not produce the same activation energies, which suggests that there is an additional temperature dependence which impacts the analysis. This can be accounted for by introducing a temperature dependent activation energy^[17,18]

$$E_A(T) = E_{A,0} - \alpha T \quad (8)$$

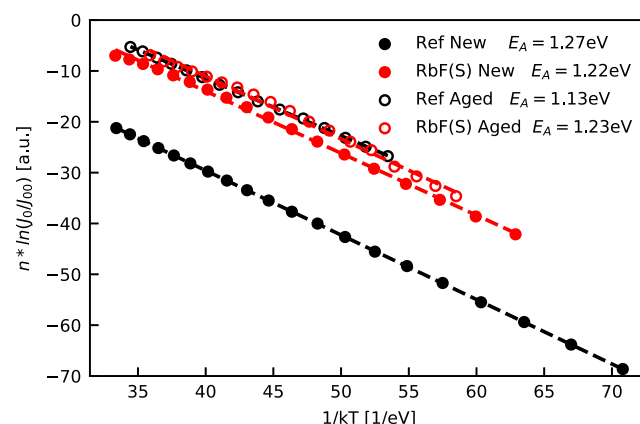


Figure 5. Arrhenius plot of $n^* \ln(J_0/J_{00})$ versus $1/kT$ with linear fits to the data. The activation energy is calculated from the slope of the fit (dashed lines).

Table 2. Calculated values from the temperature-dependent activation energy model.

		J_{00} [mA cm ⁻²]	α [meV K ⁻¹]	E_A [eV]
Ref	Fresh	3.36×10^2	1.82	1.27
	Aged	5.03×10^{-3}	2.90	1.13
RbF(S) PDT	Fresh	1.56×10^{-3}	3.00	1.22
	Aged	7.23×10^{-4}	3.30	1.23

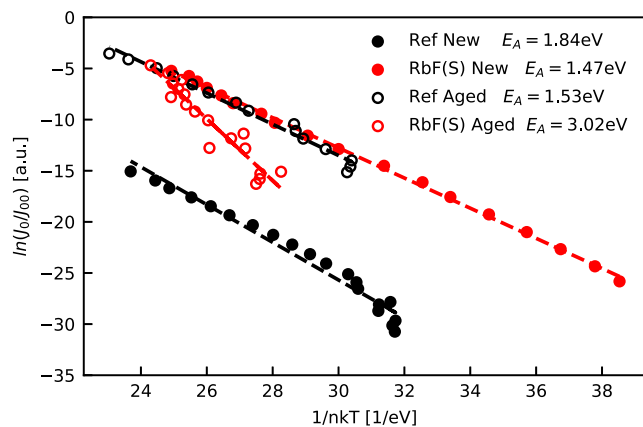


Figure 6. Modified Arrhenius plot to determine whether n is the only temperature-dependent variable. The slope of the linear fits results in activation energies that do not match those of Figure 5.

where $E_{A,0}$ is the 0 K activation energy and α is the temperature coefficient. By substituting Equation (8) into (5), a new formula can be used for analysis

$$\ln\left(\frac{J_0}{J_{00}}\right) = -\frac{E_{(A,0)}}{n(T)kT} + \frac{\alpha}{n(T)k} \quad (9)$$

Now a plot $\ln(J_0/J_{00}) - \alpha/n(T)k$ versus $1/n(T)kT$ will provide the 0 K activation energy which should match the value found using Equation (6). To create this plot, the values of α and J_{00} must be calculated through an iterative process using two more equations

$$\ln(J_0) - \frac{\alpha}{n(T)k} = -\frac{E_{A,0}}{n(T)kT} + \ln(J_{00}) \quad (10)$$

and

$$n(T) * \ln\left(\frac{J_0}{J_{00}}\right) = -\frac{E_{(A,0)}}{kT} + \frac{\alpha}{k} \quad (11)$$

Using Equation (10) a plot of $\ln(J_0) - \alpha/n(T)k$ versus $1/n(T)kT$ can be created with an initial guess of α . The intercept is then used to calculate an estimate of J_{00} which can be inserted into Equation (11). Plotting $n(T) * \ln(J_0/J_{00})$ versus $1/kT$ from Equation (11) will then provide a new value of α from the intercept. This process is repeated until both $E_{A,0}$ and α are consistent between the two plots, at which point the values of J_{00} and α can be used for further calculations.

Using the calculated values of α and J_{00} with Equation (9), the 0 K activation energy was determined for each sample (Figure 7).

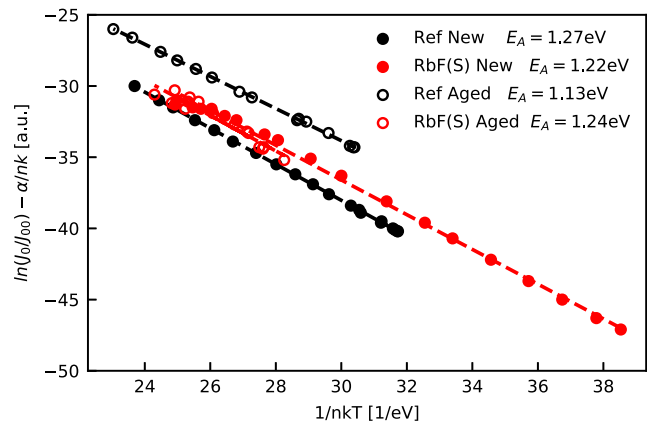


Figure 7. Arrhenius plot using the temperature-dependent activation energy model. Activation energies calculated from the slope of the linear fits agree well with Figure 5.

The activation energies were in good agreement with those found from Figure 5, improving confidence in the temperature-dependent activation energy model. The values for J_{00} , α , and E_A are listed in Table 2. Two primary mechanisms are identified as the sources of α in the literature: potential fluctuations and temperature-dependent bandgaps.^[17,18] If band-to-band recombination in the bulk is a dominant mechanism, changes in the bandgap will necessarily affect the activation energy. CIGS has been shown to have a temperature-dependent bandgap, likely contributing to α in these samples. Potential fluctuations can arise from sources such as variations in alloy composition, lattice strain, and compensating defects. They have been shown to affect α particularly when the magnitude of fluctuations is greater than kT .^[19] Assuming that the temperature dependence of the bandgap did not change significantly after aging, the changes in α after aging were likely due to increased potential fluctuations. Several studies have shown potential fluctuations to have negative impacts on device performance, particularly V_{OC} .^[4,20] As α had a greater increase in the Ref sample this is a possible contributor to its larger decline in V_{OC} after aging.

Using data from Table 2, J_0 values were calculated from Equation (9) and plotted along with the experimentally determined J_0 data (Figure 8). Because J_0 is associated with the magnitude of recombination, some conclusions about recombination in the devices can be inferred from Figure 8. While the J_0 values are close for each condition at most temperatures, the fresh RbF(S) PDT device had the lowest J_0 , particularly at low temperature. This indicates that recombination was lowest in that device, and that the PDT was effective in reducing recombination initially. This is also consistent with the increased V_{OC} value in the fresh RbF(S) PDT versus fresh Ref device. The reduction in J_0 may be related to reduced trap density which has been reported in several defect studies of RbF-treated CIGS. Karki et al. used deep-level optical spectroscopy (DLOS) to find that the concentration of a $E_V + 0.99$ eV trap to be 1.3x higher in untreated CIGS compared to RbF PDT.^[8] Helder et al. employed deep-level transient spectroscopy (DLTS) to observe that RbF PDT reduced the concentration of an $E_V + 0.4$ eV trap by a factor of 3–4x.^[21] After aging, the J_0 versus T curves converged and there was less

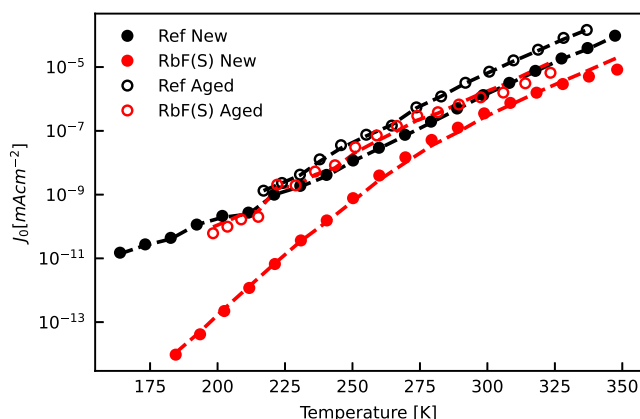


Figure 8. Comparison of experimental data (dots) with modeled (dashed lines) J_0 versus T plots using Equation (9) and data from Table 2. The modeled data agree well with experimental results.

separation between the two devices. Defect studies are needed to determine whether increased J_0 after aging is related to an increase in defect concentration, available in Mendeley Data at <https://doi.org/10.17632/ghc3p5zxh8.1>, reference number 22.

Activation energy can also be calculated from the interpolated value of V_{OC} at $T = 0$ K from the V_{OC} versus T plot (Figure 9). Using this method, all samples had activation energies near the values calculated using the J_0 data. Agreement between multiple analysis techniques of activation energies augments confidence in these results and supports the conclusion that bulk recombination is the dominant mechanism at play in these devices.

4. Conclusions

A unique RbF + S (RbF(S)) PDT for CIGS thin-film photovoltaics was tested for performance and stability against a standard reference device. After 6 months in a desiccator, both devices

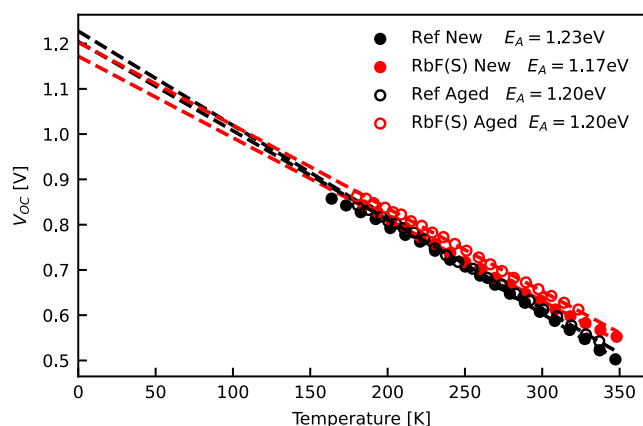


Figure 9. V_{OC} versus T plots with linear extrapolation to 0 K to calculate the activation energy. Linear fits were applied to data above 250 K to account for the low-temperature rollover effect.

showed the formation of a back contact barrier. The barrier is theorized to be a Schottky diode in reverse polarity with respect to the main diode, and the barrier height was calculated to be higher in the RbF(S) PDT device. Each device also demonstrated an increase in series resistance, which reduced FF. However, the effect was much more significant in the RbF(S) PDT device. EQE measurements also showed greater decline in bulk collection in the RbF(S) PDT device after aging, primarily for carriers generated by higher energy photons. JVT measurements were used to analyze the ideality factor and J_0 . The ideality factor values in both devices suggested SRH recombination is the dominant mechanism, particularly at normal operating temperatures. A J_0 model which accounts for temperature-dependent ideality factors and activation energies was used to calculate the diode activation energy. The diode activation energies were all near the CIGS bandgap which suggests that recombination primarily occurred in the bulk absorber. These values were supported by similar results from V_{OC} versus temperature plots. The J_0 analysis indicates that recombination was initially reduced after PDT, but after aging the benefits became negligible. Overall, while the RbF(S) PDT provides improved V_{OC} and initial efficiency, the long-term performance requires further study before becoming a commercially viable option.

Supporting Information

Supporting Information is available from the Wiley Online Library or from the author.

Acknowledgements

This work was supported in part by the U.S. Department of Energy's Office of Energy Efficiency and Renewable Energy (EERE) under Solar Energy Technologies Office (SETO) Award Number DE-EE0008755 and in part by the National Renewable Energy Laboratory, operated by Alliance for Sustainable Energy, LLC, for the U.S. Department of Energy (DOE) under Contract DE-AC36-08GO28308, in part by the U.S. Department of Energy Office of Energy Efficiency and Renewable Energy Solar Energy Technologies Office. The views expressed in the article do not necessarily represent the views of the DOE or the U.S. Government. The U.S. Government retains and the publisher, by accepting the article for publication, acknowledges that the U.S. Government retains a nonexclusive, paid-up, irrevocable, worldwide license to publish or reproduce the published form of this work, or allow others to do so, for U.S. Government purposes. This material makes use of the TOF-SIMS system at the Colorado School of Mines, which was supported by the National Science Foundation under grant no. 1726898.

Conflict of Interest

The authors declare no conflict of interest.

Data Availability Statement

The data that support the findings of this study are openly available in Mendeley Data at <https://doi.org/10.17632/ghc3p5zxh8.1>, reference number 22.

Keywords

characterization, Cu(In_xGa_{1-x})Se₂ (CIGS), recombination, thin film photovoltaics

Received: March 23, 2023

Revised: May 30, 2023

Published online:

- [1] M. Nakamura, K. Yamaguchi, Y. Kimoto, Y. Yasaki, T. Kato, H. Sugimoto, *IEEE J. Photovoltaics* **2019**, *9*, 1863.
- [2] S. A. Jensen, S. Glynn, A. Kanevce, P. Dippo, J. V. Li, D. H. Levi, D. Kuciauskas, *J. Appl. Phys.* **2016**, *120*, 063106.
- [3] P. Jackson, R. Wuerz, D. Hariskos, E. Lotter, W. Witte, M. Powalla, *Phys. Status Solidi RRL* **2016**, *10*, 583.
- [4] S. Siebentritt, E. Avancini, M. Bär, J. Bombsch, E. Bourgeois, S. Buecheler, R. Carron, C. Castro, S. Duguay, R. Félix, E. Handick, D. Hariskos, V. Havu, P. Jackson, H.-P. Komsa, T. Kunze, M. Malitckaya, R. Menozzi, M. Nesladek, N. Nicoara, M. Puska, M. Raghuvanshi, P. Pareige, S. Sadewasser, G. Sozzi, A. N. Tiwari, S. Ueda, A. Vilalta-Clemente, T. P. Weiss, F. Werner, et al., *Adv. Energy Mater.* **2020**, *10*, 1903752.
- [5] A. Kanevce, S. Paetel, D. Hariskos, T. Magorian Friedlmeier, *EPJ Photovoltaics* **2020**, *11*, 8.
- [6] P. Tsoulka, A. Crossay, L. Arzel, S. Harel, N. Barreau, *Prog. Photovoltaics Res. Appl.* **2021**, *30*, 835.
- [7] S. S. Hegedus, W. N. Shafarman, *Prog. Photovoltaics Res. Appl.* **2004**, *12*, 155.
- [8] S. Karki, S. Marsillac, P. Paul, G. Rajan, B. Belfore, D. Poudel, A. Rockett, E. Danilov, F. Castellano, A. Arehart, *IEEE J. Photovoltaics* **2019**, *9*, 313.
- [9] Series Resistance | PVEducation, <https://www.pveducation.org/pvc/drom/solar-cell-operation/series-resistance> (accessed: February 2023).
- [10] T. Kato, K. Kitani, K. F. Tai, R. Kamada, H. Hiroi, H. Sugimoto, in 32nd European Photovoltaic Solar Energy Conf. and Exhibition, WIP Renewable Energies, Munich, Germany **2016**, <https://doi.org/10.4229/EUPVSEC20162016-3AO.5.3>.
- [11] K.-J. Hsiao, J.-D. Liu, H.-H. Hsieh, T.-S. Jiang, *Phys. Chem. Chem. Phys.* **2013**, *15*, 18174.
- [12] F. Pianezzi, P. Reinhard, A. Chirilă, B. Bissig, S. Nishiwaki, S. Buecheler, A. N. Tiwari, *Phys. Chem. Chem. Phys.* **2014**, *16*, 8843.
- [13] S. H. Demtsu, J. R. Sites, *Thin Solid Films* **2006**, *510*, 320.
- [14] T. Kodalle, M. D. Heinemann, D. Greiner, H. A. Yetkin, M. Klupsch, C. Li, P. A. Van Aken, I. Laueremann, R. Schlatmann, C. A. Kaufmann, *Sol. RRL* **2018**, *2*, 1800156.
- [15] U. Rau, *Appl. Phys. Lett.* **1998**, *74*, 111.
- [16] S. A. Ringel, A. W. Smith, M. H. MacDougal, A. Rohatgi, *J. Appl. Phys.* **1991**, *70*, 881.
- [17] C. J. Hages, N. J. Carter, R. Agrawal, T. Unold, *J. Appl. Phys.* **2014**, *115*, 234504.
- [18] U. Malm, J. Malmström, C. Platzer-Björkman, L. Stolt, *Thin Solid Films* **2005**, *480–481*, 208.
- [19] J. H. Werner, J. Mattheis, U. Rau, *Thin Solid Films* **2005**, *480–481*, 399.
- [20] M. H. Wolter, R. Carron, E. Avancini, B. Bissig, T. P. Weiss, S. Nishiwaki, T. Feurer, S. Buecheler, P. Jackson, W. Witte, S. Siebentritt, *Prog. Photovoltaics Res. Appl.*, **2022**, *30*, 702.
- [21] T. Helder, A. Kanevce, A. Bauer, M. Zinßer, S. Paetel, T. M. Friedlmeier, M. Powalla, R. Kenny, J. M. Serra, *EPJ Photovoltaics* **2022**, *13*, 7.